




Drafting of two passive swimmer scale models for open-water races

B. Bolon ^{1,*}, C. Pretot,¹ C. Clanet,² F. Larrarte ^{1,3} and R. Carmigniani ¹

¹*LHSV, ENPC, and EDF R&D, 6 Quai Watier, 78400 Chatou, France*

²*LadHyX, Ecole Polytechnique, Boulevard des Maréchaux, 92120 Palaiseau, France*

³*Université Gustave Eiffel, Cité Descartes, bâtiment Bienvenue, 5 boulevard Descartes, Champs sur Marne, 77454 Marne la Vallée Cedex 2, France*



(Received 10 January 2023; accepted 12 July 2023; published xxxxxxxxx)

The interaction between two passive human swimmer scale models is investigated both experimentally and numerically. The Froude number, comparing the swimming velocity to the characteristic wave velocity, is conserved in the study. The interaction is quantified for a large range of relative positions and for three speeds corresponding to cruising, average, and sprint swimming. The associated computational fluid dynamics study using OpenFoam allows us to determine the relative positions that optimize the drafting during an open-water race: just behind a lead swimmer or at the level of the hip of a neighbor, with reductions of drag of 40% and 30%, respectively.

DOI: [10.1103/PhysRevFluids.00.004800](https://doi.org/10.1103/PhysRevFluids.00.004800)

I. INTRODUCTION AND FIELD OBSERVATIONS

In nature, animals have learned to move, swim, or fly in specific configurations in order to reduce the overall energy consumption of the group [1–3]. For example, Weihs [1] showed that young dolphin calves keep up with their mother by swimming by their side. In this configuration, Weihs calculated that the calf could gain up to 90% of the thrust needed to move at the speed of its mother, due to both Bernoulli suction and the displacement effect. Also, some birds like geese or swifts are known to fly in a V formation. The energy saving obtained by flying in a group increases their range of flight by 70% compared to a lone bird [2]. Similar conclusions exist for fish schooling: their endurance is increased by two to six times [3]. These situations are called drafting. In sports, drafting is observed in team sports (team pursuit in cycling, for example), or when racing against other athletes: running, swimming, car racing, or cycling. The general idea is that an athlete can benefit from a drag reduction when being behind another one. Therefore the draft athlete produces less effort than their opponent to move at the same speed. This energy savings can make a difference in the outcome of a race. It exists in various disciplines as illustrated in Fig. 1. Drafting has been studied in various sports [4–6]. For example, in cycling, Blocken *et al.* [4] studied the drafting effect on two cyclists numerically, highlighting the fact that the trailing cyclist encounters a reduction of his drag from 13% to 27% depending of his position on the bike and that this reduction decreases with distance.

Blocken *et al.* [5] also measured drag on scale models in peloton formation due to wind-tunnel testing, showing that there are preferential positions in a peloton that allow a cyclist to encounter minimum drag. It is also a well-known phenomenon in racing cars. For instance, computational fluid dynamics (CFD) studies in NASCAR (National Association for Stock Car Auto Racing) races showed a drag reduction for the trailing car [6]. All the previously mentioned sports are in air. In swimming, athletes move at the interface between two fluids: air and water, which makes drafting in swimming specific because of the waves created at this interface. Different studies have measured

*baptiste.bolon@enpc.fr

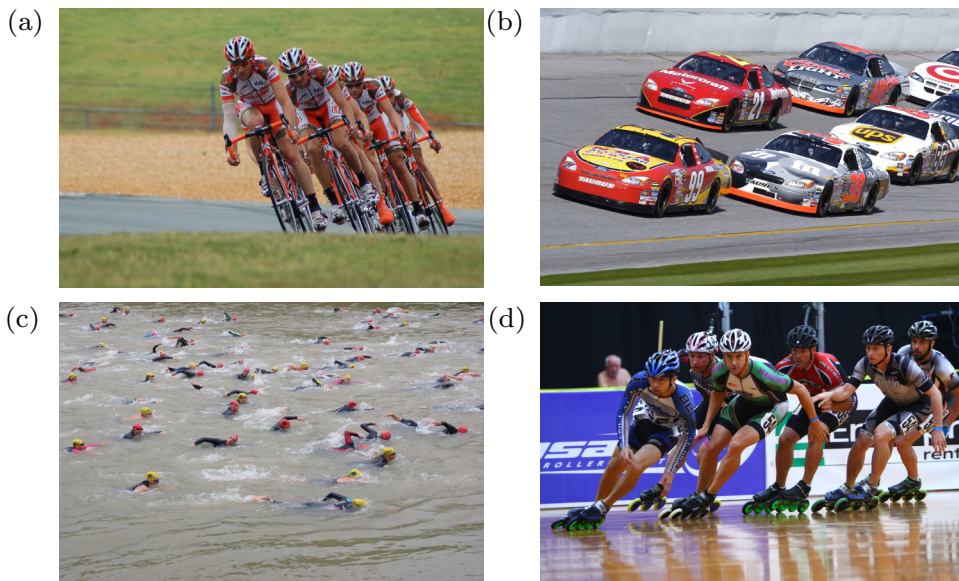


FIG. 1. Examples of drafting situations in various sports: (a) Peloton formation in cycling; (b) NASCAR racing; (c) open-water swimming; (d) speed skating (all pictures copyright-free).

43 physiological parameters and their evolution in drafting situations [7–9]. These articles draw the
 44 conclusion that drafting has a positive impact on physiological parameters such as a reduction
 45 of the concentration of blood lactate, a reduction in oxygen uptake and heart rate, and a reduced
 46 perceived exertion on the Borg scale (which is a way of measuring physical activity intensity level
 47 based on physical sensations [10]). As a consequence, draft swimmers will face less physical fatigue
 48 than isolated swimmers. Moreover, Janssen *et al.* [9] also have shown a positive correlation between
 49 passive drag reductions in drafting formation and physiological benefit in active swimming in those
 50 same formations. There are also numerical papers that study drag forces and drag coefficients
 51 on passive swimmers [11,12]. They suggest that the drafted swimmer encounters reduced drag
 52 compared to the leading swimmer, which can explain the evolution of physiological parameters
 53 mentioned before. The wave field created by a passive leading swimmer has been studied by Yuan
 54 *et al.* [13] using a potential theory approach and neglecting the wake produced by the swimmers.
 55 They found that a draft swimmer following a leader could encounter a drag increase or decrease
 56 depending on the distance separating the two swimmers. This may be due to the transverse waves
 57 generated by the lead swimmer. Indeed, they are not disturbed by the turbulent wake, which was
 58 neglected in the first place when choosing a potential approach. Finally, some works try to actually
 59 measure drag during drafting experimentally. For example, Westerweel *et al.* [14] did some drag
 60 measurements on scale models and concluded that the drag reduction could be up to 40% for the
 61 draft swimmer. Our goal is to determine the relative positions of swimmers that allow them to
 62 make the most of drafting during open-water races. The study is conducted on passive scale models,
 63 which allows us to study a wide range of race configurations. First, we present our experimental and
 64 numerical setups. Then we display our results for in-line swimming and for side-by-side swimming.

65 II. EXPERIMENTAL AND NUMERICAL SETUP

66 A. Experimental setup

67 All the experiments took place in the Electricité de France (EDF) Lab facility in Chatou, France.
 68 The scale models are fixed in an open water channel which is 80 m long, 1.5 m wide, and 1.2 m
 69 deep. A scheme of the facility is shown in Fig. 2.

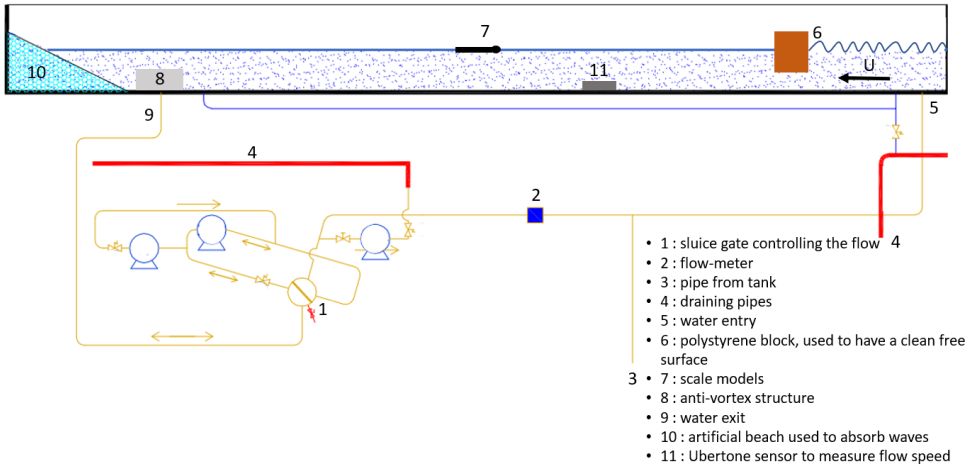


FIG. 2. Schematic view of the flume in the longitudinal vertical plane.

The tank is filled with water up to an height $h = 0.7$ m (discussed later). The models position is controlled using a motored arm with millimetric precision. The model depth is fixed throughout the experiment. The position is chosen such that the swimmer's head is just below the surface for the standing water case (no current in the tank) for repeatability. In this configuration, the swimmer's shoulders are slightly out of water. Once the pump is running the water height increases slightly (about 2 cm). In the running configuration, the swimmer is then fully submerged. We use an antivortex structure at the water exit in order to prevent air from penetrating the pump. We choose to study three speeds of the flow, in order to represent different swimming paces characteristic of open water races: 1.25, 1.5, and 1.7 m/s for human swimmers. In the following, they are respectively called the cruising, average, and sprint speeds. To determine the corresponding speed of the flow in the flume for our scaled experiment, we use a Froude similitude:

$$Fr = \frac{V}{\sqrt{gL}}, \quad (1)$$

with V the velocity of the flow, g the gravity constant, and L the length of a swimmer. We obtain $Fr = 0.28, 0.34,$ and 0.38 for the three swimming speeds chosen, respectively, using 2 m as the length of a human swimmer. We work in the deep-water limit to mimic conditions encountered by actual swimmers in races. We note k the wave number of the transverse waves created by the scale model. We have $k = 2\pi/\lambda$ where λ is the wavelength. According to [15], we are in a deep-water regime if $kh \gg 1$, where h is the water height. The order of magnitude of λ will be the length of the scale model. Since the maximum flow in the flume is 1000 L/s, we choose the length of our

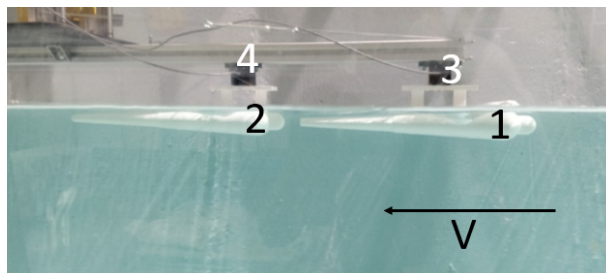


FIG. 3. Experimental setup: (1) Lead scale model, (2) draft scale model, (3) and (4) 1D shear force sensors.

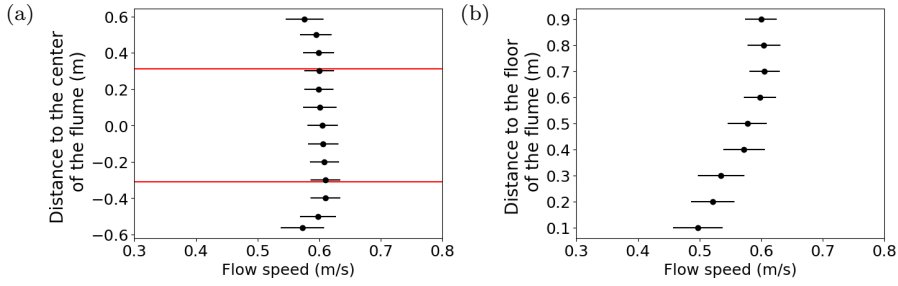


FIG. 4. Streamwise velocity profile in the flume for a given flow. (a) Profile along the transverse axis of the flume. (b) Profile along the vertical axis of the flume.

88 scale models to be 0.4 m and the water depth to be 0.7 m, in order to fulfill both Froude numbers
 89 conditions and deep-water constraint. Knowing the length of our model, we determine the speeds of
 90 the flow in our flume due to the Froude similitude: 0.56, 0.67, and 0.75 m/s. We can then calculate
 91 the Reynolds number of our flow, defined as

$$\text{Re} = \frac{VL}{\nu}, \quad (2)$$

92 where ν is the water kinematic viscosity. For the smallest speed, we obtain $\text{Re} = 2.24 \times 10^5$. For
 93 human swimmers, taking $L = 2$ m and $V = 1.5$ m/s (typical open water swimming speed), we
 94 obtain $\text{Re} = 3 \times 10^7$. Both are large enough to assume that a turbulent regime is reached. Details
 95 about Reynolds independence of the drag coefficient are provided in Appendix C. A close-up view
 96 of the setup is shown in Fig. 3.

97 Models are 3D printed, using polylactic acid and using a 0.0004 m diameter nozzle. The
 98 geometry of the model is available in the Supplemental Material [16]. Drag forces are measured
 99 using 1D shear force sensors designed by Phyling [17]. They are shown in Fig. 3, as items 3 and 4.
 100 The force measured with the sensors goes from 0.2 to 0.9 N depending on the configuration studied.
 101 Details are provided in Appendix B. Drag is acquired at 100 Hz during 20 s, repeated six times,
 102 and averaged for each configuration studied. Speeds are measured with a UB-flow acoustic profiler
 103 from Ubertone. Velocity measurements were made to assess velocity variation in the z direction and
 104 y direction, shown in Fig. 4. From the profile made along the transverse axis, we deduce that the
 105 flow speed remains constant in the measurement zone (delimited the two red horizontal lines). The
 106 asymmetry of the profile can be explained by the fact that one side of the flume is a rough wall,
 107 while the other side is made of smooth glass.

108 Convention of the forces is presented in Fig. 5. F_x stands for the force in the direction of the flow,
 109 i.e., drag force; F_y stands for the force in the perpendicular direction to the flow, in the plane of the

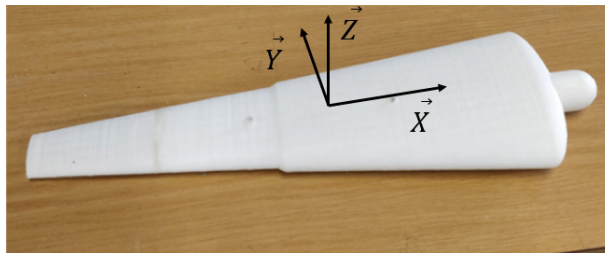


FIG. 5. Frame of reference.

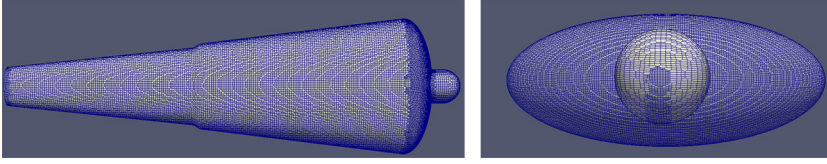


FIG. 6. Zoomed view of the mesh around a model.

water surface, i.e., side force; and F_z stands for vertical force. In this work we focus on drag and side forces. 110
111

B. Numerical method 112

Numerical studies are done using OpenFoam software v2012 [18] and *interFoam* solver (which 113
uses a volume of fluid method). A mesh was created using the *blockMesh* command. The domain is 114
12 m long, 2 m large, and 5 m high. Six refinement boxes are used to refine the mesh in the regions 115
of the scaled models, due to *topoSet* and *refineMesh* commands. Finally, the scale models' geometry 116
is exported into the mesh with the *snappyHexMesh* command. A zoomed view of the mesh around a 117
model is displayed in Fig. 6. 118

A speed is imposed at the inlet of the mesh in order to recreate the conditions of our experiment. 119
On the side, bottom, and top faces of the domain, a wall condition is imposed. At the outlet, a *zero- 120
Gradient* pressure condition is imposed. We use a *k- ω* SST turbulence model: a blending function 121
activates either the Wilcox model near walls or the *k- ϵ* model in a free stream, which ensures that the 122
appropriate model is used for the entire flow field. The parameters used for this turbulence model are 123
those of the OpenFoam documentation [19]. Fluids are considered incompressible. For water, we use 124
 $\rho = 998.8 \text{ kg/m}^3$ and $\nu = 1 \times 10^{-6} \text{ m}^2/\text{s}$. For air, we use $\rho = 1.2 \text{ kg/m}^3$ and $\nu = 1.5 \times 10^{-5} \text{ m}^2/\text{s}$. 125
The time step used is $dt = 0.01 \text{ s}$ for lowest speeds and 0.001 s for the higher speed to ensure 126
convergence. There are approximately 4 million cells in our OpenFoam cases. Each case represents 127
36 h/CPU. To assert convergence, we looked at the evolution of the drag force computed at each 128
iteration by OpenFoam. An example is shown in Fig. 7. Moreover, at each time step we make sure 129
that both pressure and alpha (volume of water in each cell) had converged. This is made by looking 130
at the value of residuals in OpenFoam. To assert spatial convergence, we performed different cases 131
with different mesh cell sizes. 132

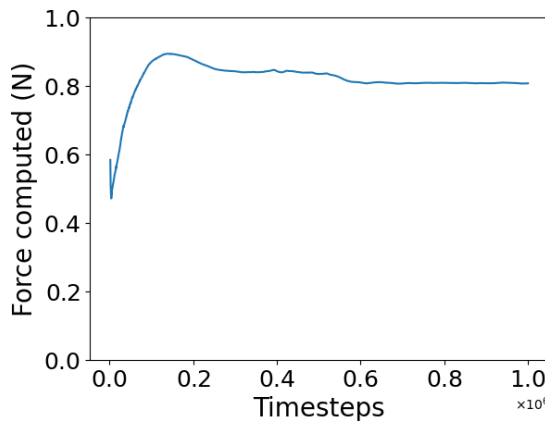


FIG. 7. Evolution of the drag force computed during a CFD simulation.

III. RESULTS

A. In-line swimming

1. Measurements

For in-line swimming, we define L_x as the distance between the head of the two models. Considering that the frame of reference, defined in Fig. 5, is attached to the lead scale model, L_x is negative in this section and $L_x/L < -1$ to ensure there is no collision between models. The definitions and conventions are shown in Fig. 8(a). We introduce the drag coefficient of a lone swimmer as

$$C_{d,0} = \frac{F_x}{\frac{1}{2}\rho SV^2}, \quad (3)$$

where F_x is the drag force, ρ is the water density, S is the frontal area of a swimmer, and V is the speed of the flow. The values of $C_{d,0}$ are 0.58 ± 0.052 , 0.62 ± 0.056 , and 0.60 ± 0.054 for $V = 0.56, 0.68,$ and 0.75 m/s, respectively. We also define the normalized drag as

$$\overline{C_d} = \frac{C_d}{C_{d,0}}, \quad (4)$$

where C_d is the drag coefficient measured during the in-line swimming experiment. With this definition, a configuration where $\overline{C_d}$ is smaller than 1 is advantageous for the swimmer compared to swimming alone, and disadvantageous if it is higher than 1. The experiment consists in measuring drag for the lead and draft scale models, for a wide range of L_x and for the three speeds chosen in the previous section. The results displayed in this section in Figs. 8(b)–8(d) are the evolution of the normalized drag with the nondimensional distance between models for both the leading model and

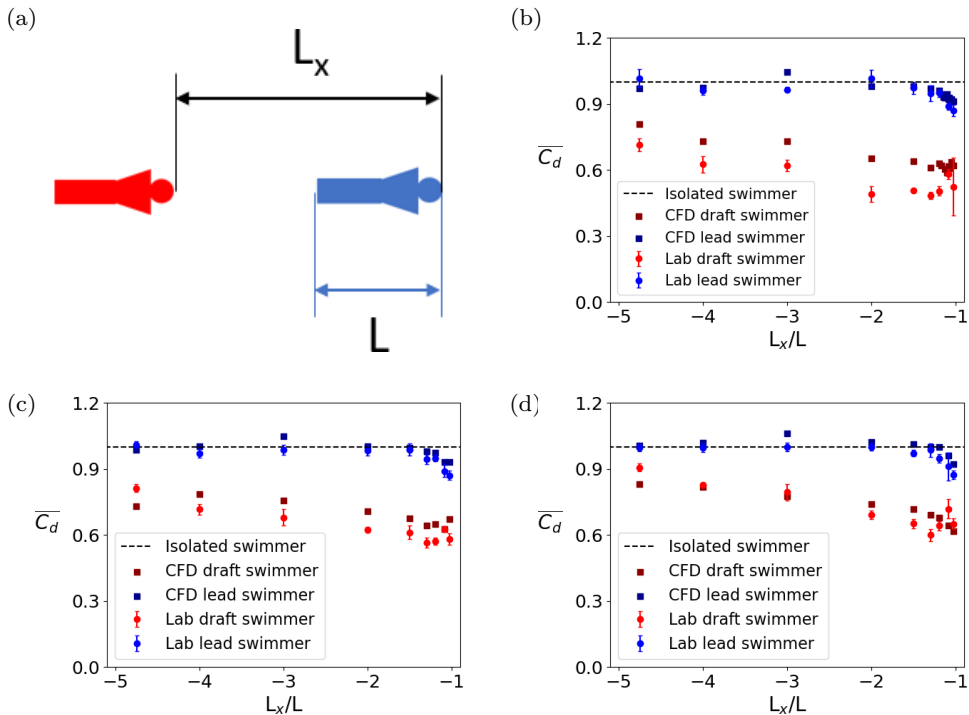
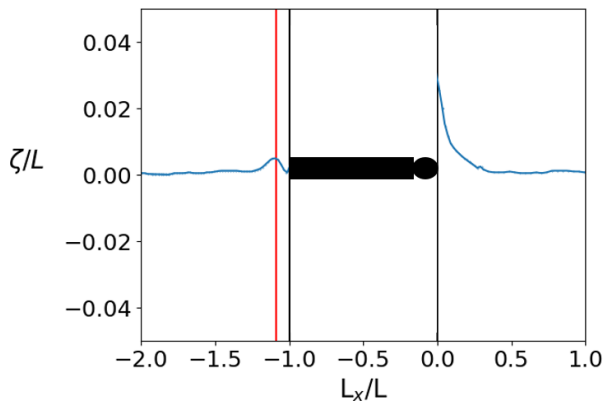


FIG. 8. Drag measurements for three Froude numbers for in-line swimming. (a) Schematic view of in-line swimming setup. (b) In-line swimming results for $Fr = 0.28$. (c) In-line swimming results for $Fr = 0.34$. (d) In-line swimming results for $Fr = 0.38$.

FIG. 9. Free surface profile, lone scale model, $Fr = 0.28$.

draft model. We show both laboratory measurements and OpenFoam results. The error bar stands for the 95% reliability interval.

For the leading model, our results show that it encounters a drag reduction, up to 15%, when closely followed by another one. Quantitatively, its normalized drag is smaller than 1 for nondimensional distances in the interval $[-1.5, -1]$. That is to say when it is followed at less than half a body length. For the draft model, our measurements show a big reduction of its drag, up to 45% in some configurations, when located right behind the leader. Then the reduction of drag decreases as the distance between models increases. However, the reduction of drag still exists at four body lengths behind the leader: 30%, 20%, and 10% reductions for $Fr = 0.28, 0.34$, and 0.38 , respectively. These results are similar to those reported in previous studies in various sports: [4,11,14].

2. Discussion of results and free-surface analysis

In the experimental results, shown in Figs. 8(b)–8(d), a systematic increase of drag is noticeable for the second closest position for the draft model. This corresponds to the position $L_x/L = -1.0875$ and is outlined by the vertical red line in Fig. 9. This fluctuation in the drag reduction of the drafter is not observed for fully submerged models in other sports and might be due to the presence of the interface between the two fluids. This fluctuation of drag reduction for the drafter appears to be similar to the wave effect reported by Yuan *et al.* [13] in their potential approach. The free-surface deformation, ζ , for a lone scale model along the $y = 0$ axis was computed using OpenFoam and is shown in Fig. 9. The free-surface deformation shows a negative gradient ahead of the swimmer similarly to [13]. Behind the swimmer, we can see a single bump with a maximum near $L_x/L = -1.0875$. This wave positive gradient in the x direction might explain the increase in drag observed in this configuration.

However, some of our results are in discordance with [13], for both drag measurements and free-surface state. Indeed, [13] highlights that for in-line swimming, there is an alternation of positions with reduction of wave drag and positions with increase of wave drag depending on the value of L_x , whereas in our experiments all the configurations studied show a drag reduction for the draft scale model. Concerning free surface, [13] shows a transverse wave region, whereas in our case, there is only one significant wave behind the scale model because of its turbulent wake. Those differences may be due to the potential approach chosen by [13], when both our experiments and CFD simulations are in a turbulent regime, which is closer to reality for human swimmers.

B. Side-by-side swimming

1. Drag forces

During open-water races, swimmers are often side by side either to pass an opponent, swim around a turn buoy, or be at the feeding station. Moreover, it is simpler for them to see where they

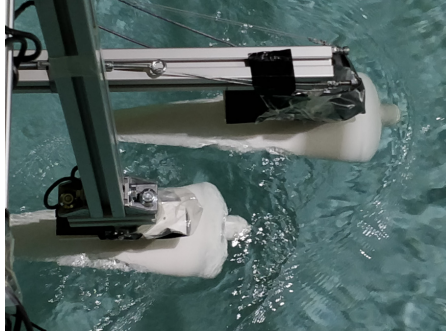


FIG. 10. Side-by-side swimming setup, top view.

184 are going when side by side, in order to follow a beeline between turn buoys. That is the reason why
 185 we also study side-by-side swimming configurations. The experimental setup is shown in Fig. 10.
 186 We define L_x as the distance between the two heads of our models in the direction of the flow and
 187 L_y as the distance between the two heads in the direction perpendicular to the flow, as shown in
 188 Fig. 11(a). With this definition, the minimum value of L_y is 12 cm as models are 12 cm large at
 189 the shoulder level. In the first set of experiments, L_y remains constant: $L_y = 12.5$ cm, whereas L_x
 190 varied. We chose this value for L_y , as it is the minimum reachable value, taking into account that
 191 actual swimmers cannot swim too close from each other due to their arms moving. The influence of
 192 L_y is studied in the next sections.

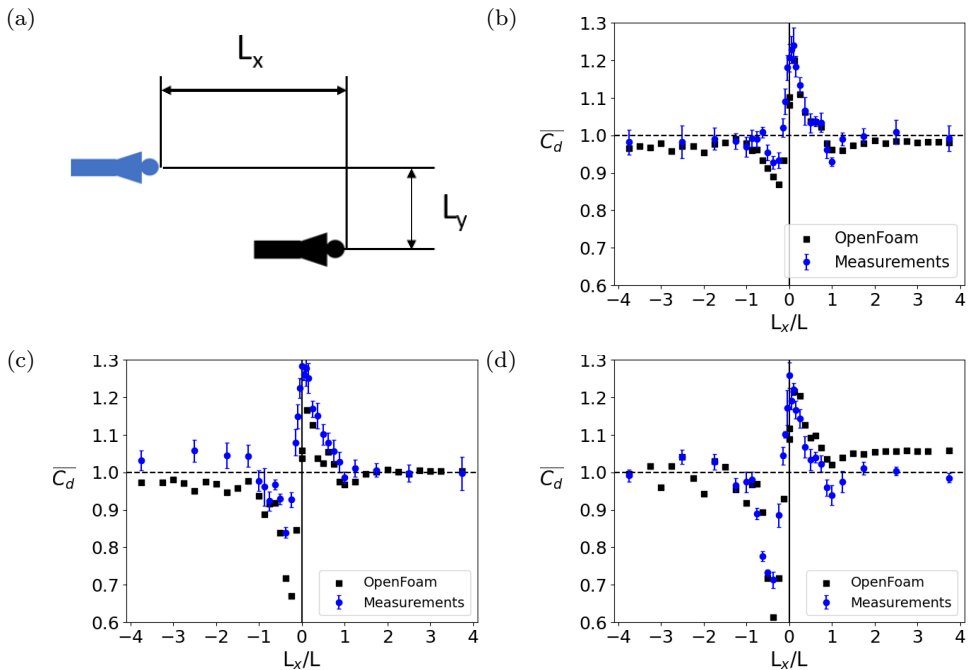


FIG. 11. Drag measurements for three Froude numbers for side-by-side swimming with $L_y/L = 0.3125$. (a) Schematic view, side swimming. (b) Side swimming results for $Fr = 0.28$. (c) Side swimming results for $Fr = 0.34$. (d) Side swimming results for $Fr = 0.38$.

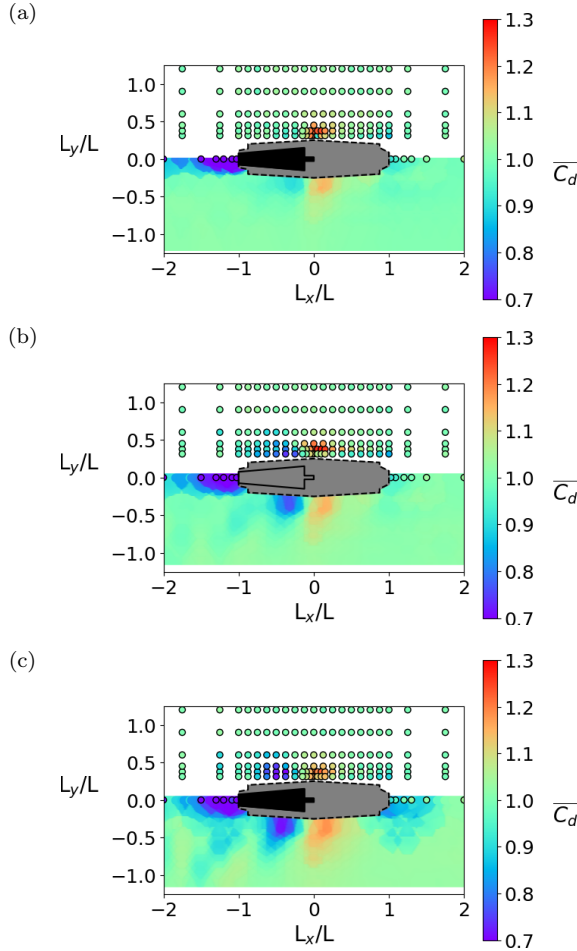


FIG. 12. 2D map of the drag, comparing laboratory and CFD data. (a) 2D drag map for $Fr = 0.28$; (b) 2D drag map for $Fr = 0.34$; (c) 2D drag map for $Fr = 0.38$.

In Figs. 11(b)–11(d) we present the evolution of normalized drag [defined as in Eq. (4)] with nondimensional distance L_x/L . For instance, a nondimensional distance L_x/L of 0 means that scale models are perfectly side by side, and -1 means that the head of one model is at the feet of the other one. Moreover, a nondimensional distance L_y/L of 0.3 means that models' shoulders are touching, and a greater value means that models do not touch each other. We show results from both laboratory experiments (blue dots) and OpenFoam results (black squares). The error bar stands for the 95% reliability interval. We notice that for the three speeds, the normalized drag is maximum when models are aligned with no gap (meaning $L_x = 0$). Moreover, this maximum does not seem to be affected by the speed: indeed, it stays between 1.25 and 1.3 for the three speeds. As the normalized drag is higher than one, that means that in this configuration, scale models encounter a drag larger than the one they experience alone. As a consequence, in a race, swimmers should avoid this side-by-side configuration if they want to preserve their physical strength and reduce fatigue. However, they can also try to impede the passing of an opponent and wear them out by blocking them in this configuration. We can also observe, for each speed, a minimum of drag. This minimum happens for a nondimensional distance between -0.3 and -0.5 , meaning that the measured model is at the hip of its neighbor. Contrary to the maximum of drag, the value of the minimum depends of the speed

193
194
195
196
197
198
199
200
201
202
203
204
205
206
207
208

209 of the flow. It's equal to 0.9, 0.8, and 0.7, respectively, for $Fr = 0.28, 0.34,$ and 0.38 . Those value
 210 of the normalized drag highlights that this position is the best for swimmers who want to save their
 211 energy and cannot swim in line. Moreover, we can see that the minimums of drag for side-by-side
 212 swimming are higher than the minimums for in-line swimming. If swimmers have the choice and
 213 want to preserve themselves, they should thus swim in line behind a leader. Finally, we observe that
 214 laboratory data and CFD data match pretty well: the same phenomena occur at the same locations
 215 and with the same intensity.

216 **2. Force map**

217 For each speed, and for different values of L_y ($L_y/L \in [0.3125, 0.375, 0.45, 0.6, 0.9, 1.2]$), we
 218 perform drag measurements, as we did in the previous section. The aim here is to characterize the
 219 drag force encountered by the scale model in a 2D space, in order to have a better understanding
 220 of the positions that could be advantageous or disadvantageous. We also extend our CFD study
 221 with OpenFoam to configurations not studied experimentally. Our results are shown in Fig. 12. The
 222 black contour is a schematic view of one model. The gray zone represents the part of the 2D space
 223 where the model cannot be without overlapping its neighbor. Each dot represents a measurement
 224 point and is the location of the scale model's head relatively to the black model on the graph. The
 225 color of the dot represents the intensity of the drag force. Each figure is divided in two parts: the
 226 top part (discrete points) is laboratory measurements, and the bottom part (continuous data) is the
 227 OpenFoam results and interpolation.

228 First, we observe that the location of the advantageous and disadvantageous configurations seem
 229 to be independent from the speed of the flow. We also notice that, when $L_y/L > 0.75$ (meaning
 230 when the lateral distance between models is more than three quarters of a body length), there is no
 231 more drafting phenomenon as the model's drag coefficient is equal to the one of a solitary model.
 232 This confirms that the best configuration to encounter a minimal drag is to swim right behind the
 233 feet of a leading swimmer or to be at the hip of an opponent. The worst configuration, where the
 234 drag is maximum, is when swimmers are perfectly side by side.

235 **3. Free-surface analysis**

236 Using OpenFoam simulations, we are able to plot the free surface of the flow, for a lone scale
 237 model. The results are shown in Fig. 13(a) and can be qualitatively compared to the experiment
 238 in Fig. 13(b). Comparing the free-surface height with the advantageous and disadvantageous
 239 configurations highlighted in Fig. 12, we can say that, for side swimming, reductions of drag seem
 240 to be mainly due to swimming on a negative gradient, projected in the x direction, wave. This can
 241 be confirmed by looking at a free-surface profile for a chosen value of L_y . An example is shown
 242 in Fig. 14. We plotted the head position for the maximum (gray vertical line) and the minimum of

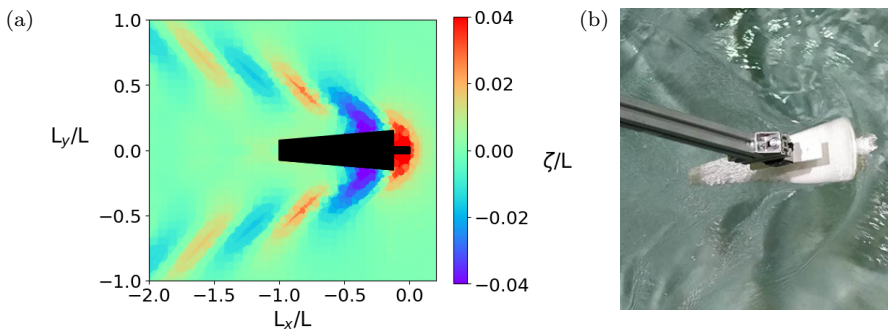


FIG. 13. (a) Free-surface height for $Fr = 0.34$, obtained with OpenFoam. (b) Qualitative experimental wavefield for $Fr = 0.34$.

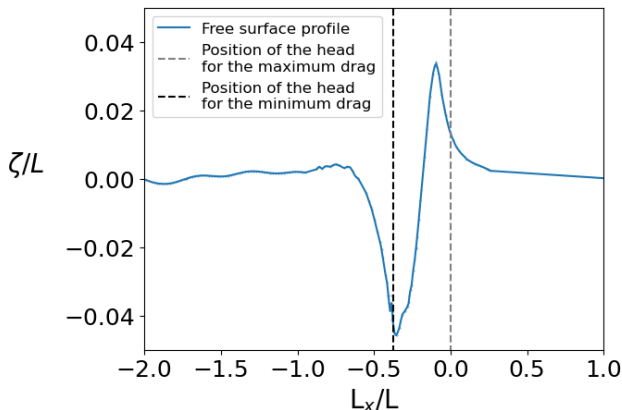


FIG. 14. Free-surface height for $Fr = 0.34$, $L_y = 0.015$ m, obtained with OpenFoam.

drag (black vertical line). We observe that for the minimum of drag, a large part of body is facing a negative gradient, projected in the x direction, wave: the model is “surfing” the wave created by its neighbor, which explains the reduction of drag measured in both the laboratory and CFD. On the other hand, for the maximum of drag, the model is facing both a positive and negative wave gradient, projected in the x direction. As a consequence, the increase of drag does not come solely from the wave gradient. We can explain the increase of drag when models are close to each other: the wave created by each model in its upstream, as seen next to the head in Fig. 13(a), interacts to create a bigger wave. We suppose this, as a consequence, increases the wave drag of both models and therefore increases their total drag.

To confirm or reject our assumptions about the influence of free surface, we complete our work by computing three different fully submerged cases: an lone model, two models head to head corresponding to the maximum of drag found in Fig. 11 with $L_y/L = 0.3125$, and two models with one at the hip of the other with $L_y/L = 0.3125$ and $L_x/L = -0.4$, corresponding to the minimum of drag found in Fig. 11. For each case we compute the normalized drag (the drag divided by the drag of a lone and fully submerged model).

The results shown in Table I highlight the fact that we do not have anymore the variations of drag observed for the free-surface case. Moreover, the drag force encountered by the models is roughly the same for all the submerged cases studied and equal to the drag of a lone submerged model. This confirms that the variations of drag shown in Figs. 11 and 12 can be explained by waves and the free-surface effect in our work.

4. Side forces

To quantify side forces, we use the same sensors as for drag force measurements. We use the following convention: a positive force means that the scale model studied is repulsed by its neighbor, and a negative force means it is attracted by its neighbor, as shown in Fig. 15(a). We define the side

TABLE I. Results for CFD fully submerged cases.

Case studied	Normalized drag
Alone model	1.000 ± 0.008
Side-by-side model	1.015 ± 0.006
Hip lead model	1.033 ± 0.004
Hip draft model	1.023 ± 0.009

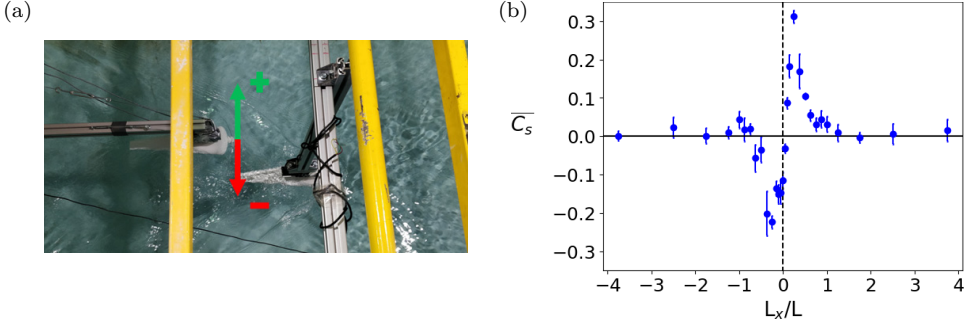


FIG. 15. Side force measurements for $Fr = 0.38$ and $L_y/L = -0.3125$: (a) Side forces conventions; (b) lab results.

267 coefficient as

$$C_s = \frac{F_y}{\frac{1}{2}\rho S V^2}. \quad (5)$$

268 We also define the normalized side coefficient in the same way as for the normalized drag
269 coefficient:

$$\overline{C}_s = \frac{C_s}{C_{d,0}}. \quad (6)$$

270 Results are displayed in Fig. 15(b).

271 We observe that when a model is slightly in front of another one, it encounters a positive
272 transverse force, which means it is repulsed by its neighbor. Moreover, when one is slightly behind
273 another model, it encounters a negative transverse force, meaning it is attracted by its neighbor.
274 If we look at the configuration shown in Fig. 15(a), we conclude that both models will encounter a
275 force which drags them towards their right. As a consequence, even if transverse forces are low
276 compared to drag forces, swimmers will still have to compensate in order to swim in a straight line,
277 which is crucial in open-water swimming in order to use a beeline between two turn buoys.

278 5. Evolution of drag with lateral distance L_y

279 To quantify the interaction zone between swimmers, we decided to study numerically the
280 influence of the lateral distance between models noted L_y , as defined in Fig. 11(a). For this study,

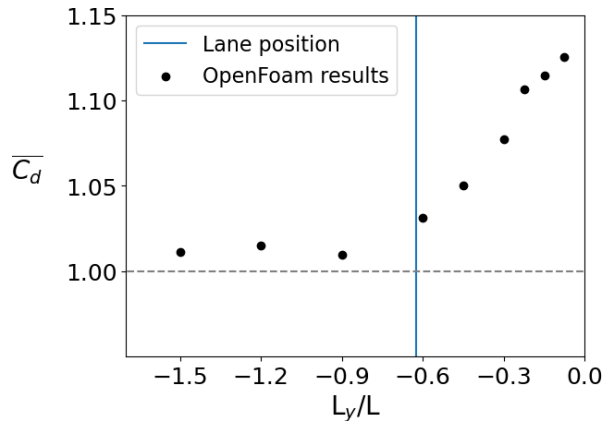


FIG. 16. Influence of lateral distance on drag for $Fr = 0.38$, $L_x/L = 0$, results obtained with OpenFoam.

models are perfectly side by side ($L_x = 0$) and we change only L_y , separating them. Results are shown in Fig. 16. As shown in the figure, when models are really close to each other, drag is maximum. Then, as the lateral distance between them increases, the drag they encounter decreases to finally reach a stable value for great distances, that is to say, more than 0.75 body length. This may raise the idea that one should move aside when passing an opponent in order to reduce the encountered drag.

Moreover, the blue vertical line represents the position of the swimming-pool lane if both swimmers are located at the exact center of their swimming lane, which represents a distance of 2.5 m in real life. This might justify the empirically chosen width of a swimming lane in competitions. Moreover, it outlines the crucial role of swimming lane ropes in competition.

IV. CONCLUSION

We used laboratory measurements on scale models to study drafting in both in-line and side-by-side swimming. We observe that the best configuration to benefit from drag reduction in a two-swimmer configuration is to follow as closely as possible a leading swimmer. Moreover, being at the hip level of an opponent is also a great way to encounter a reduction of drag, by riding the wave created by the opponent. On the other hand, being at the head level of an opponent makes both swimmers encounter a maximum drag, superior to one of an isolated swimmer. The CFD simulations confirm the experimental results and allow us to extend the study to quantify the region of interaction between swimmers. There is a good correlation between CFD results and laboratory measurements. CFD also helped us to explain phenomena observed during experiments due to free-surface analysis. However, the impact of active swimming on our drag measurements is still unknown and will have to be studied in a future work. We also need to study peloton configurations, as they often occur in open-water races.

APPENDIX A: COMPARISON WITH A BUOYANT CASE

To evaluate the effect of buoyancy, we compare our results to those of Westerweel *et al.* [14]. Indeed, our models are not free to move on the vertical axis, whereas it was possible in their work for one model when the other one was fixed.

The setup is very similar to our setup: scaled models are placed in a flume which is 3 m long and 1.5 m wide. We work at the same Froude number, $Fr = 0.28$. There are slight geometry differences between our scaled models and those used here. Moreover, in this study, contrary to ours, models are buoyant and therefore can move along the vertical axis, which is closer to real human swimmers. This setup is shown in Fig. 17(a).

The comparison between nonbuoyant and buoyant cases is shown in Fig. 17(c). In this graph, nonbuoyant results are the square points and the crosses are buoyant results. For the leader (blue squares and black crosses), we observe the same phenomenon. The leader encounters a drag reduction when closely followed by an opponent. This reduction is about 10% and seems not to be affected by buoyancy. For the draft model (red squares and gray crosses), we both observe a big drag reduction, but it is more important in the buoyant experiment: 55% vs 45% in our case. This difference can be explained by an increase of the uplift of the draft model. As a conclusion, we found similar results for the lead model and less drag reduction than Westerweel for the draft model. The model of a completely buoyant swimmer may be a little exaggerated and as a consequence the uplift bigger than for an actual swimmer. So the drag reductions may be overevaluated. However, the truth may be found in between our experiments and his, as we observe the same tendencies and physical phenomena.

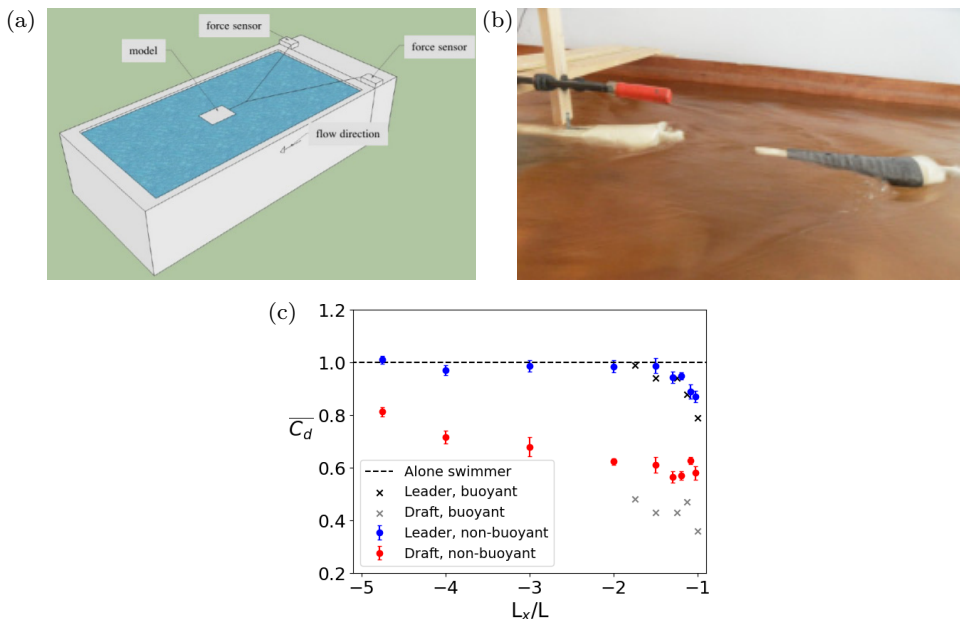


FIG. 17. Comparison with Westerweel's buoyant case [14]: (a) Westerweel's experimental setup; (b) two scale models setup; (c) comparison of the results. Westerweel *et al.* data extracted from [14].

APPENDIX B: MULTIVARIATE ERROR ANALYSIS

325

326 In this section, we define u as the measurement error and U as the 95% reliability interval. We
 327 therefore have $U = 2u$. We also define the drag coefficient as in Eq. (3). The force F is obtained
 328 by multiplying the tension A measured by the sensor with a constant conversion coefficient k .
 329 Moreover, the frontal area S is an ellipse, meaning we have $S = \pi ab$, where a and b are the half of
 330 big and small axes of the ellipse. Therefore, the drag coefficient is obtained as follows:

$$C_d = \frac{kA}{\frac{1}{2}\rho\pi abV^2}. \quad (\text{B1})$$

331

We can then apply the formula for error propagation:

$$\frac{u(C_d)}{C_d} = \sqrt{\left(\frac{u(k)}{k}\right)^2 + \left(\frac{u(A)}{A}\right)^2 + \left(\frac{u(\rho)}{\rho}\right)^2 + \left(\frac{u(a)}{a}\right)^2 + \left(\frac{u(b)}{b}\right)^2 + \left(\frac{u(V^2)}{V^2}\right)^2}. \quad (\text{B2})$$

332

Then we have a look at each term of the right member:

333

334

335

336

337

338

339

340

341

342

343

344

(i) k : k is the coefficient which converts the tension measured by the force sensor in volts into a force in newtons. The sensors have a range of -5 to 5 N. To obtain k , for both sensors, we perform a calibration before the beginning of the experiments. This consists in suspending various known masses to the sensor (fixed to the swimmer as in the experiment) using a pulley. An example of the calibration result is shown in Fig. 18.

We obtain for the two sensors, $k_1 = 1.239$ N/V, $u(k_1) = 0.0095$ N/V and $k_2 = 1.424$ N/V, $u(k_2) = 0.02$ N/V.

(ii) A : A is the mean tension measured during six trials of 20 s. Then $u(a)$ is obtained by computing the standard deviation of the mean tension signal. A and $u(A)$ depend on the trial and are computed for each trial.

(iii) ρ : Water in the flume is at ambient temperature, that is to say, between 15 and 20 °C. We have $\rho(T = 15$ °C) = 999.77 kg/m³ and $\rho(T = 20$ °C) = 998.29 kg/m³. Considering a uniform

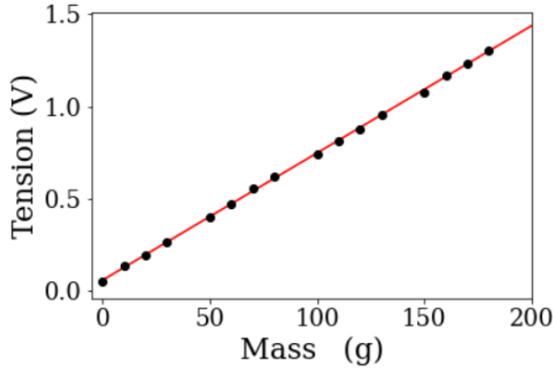


FIG. 18. Results of sensor calibration: tension obtained for different suspended masses.

distribution of temperatures during the various trials, the mean value is $\rho = 999.03 \text{ kg/m}^3$ and $u(\rho) = U(\rho)/2 = 0.37 \text{ kg/m}^3$. 345

(iv) a : $a = 0.06 \text{ m}$ in the stl file. According to the properties of the 3D printer (RAISE 3D Pro2 Plus), we have $u(a) = 10 \text{ }\mu\text{m}$. This is independent from the trial. 347

(v) b : $b = 0.025 \text{ m}$ in the stl file. According to the properties of the 3D printer (RAISE 3D Pro2 Plus), we have $u(b) = 10 \text{ }\mu\text{m}$. This is independent from the trial. 349

(vi) V^2 : First, we use that $\frac{u(V^2)}{V^2} = 2\frac{u(V)}{V}$. Speed was not measured at each trial, but each time flow speed was changed in the flume. Therefore, for each targeted speed we give a mean value and U the 95% reliability interval given by the standard deviation of all the speeds obtained for one targeted speed. For V targeted at 0.56 m/s : $V = 0.561 \text{ m/s}$, and $u(V) = 0.005 \text{ m/s}$. For V targeted at 0.67 m/s : $V = 0.678 \text{ m/s}$, and $u(V) = 0.006 \text{ m/s}$. For V targeted at 0.75 m/s : $V = 0.750 \text{ m/s}$, and $u(V) = 0.006 \text{ m/s}$. 351

We compute the multivariate error for one given example: a trial of a single swimmer at 0.56 m/s . We obtain $\frac{u(C_d)}{C_d} = 0.045$. For this trial, we have $C_d = 0.580$. Moreover we use that $U(C_d) = 2u(C_d)$. Finally, we obtain $C_d = 0.580 \pm 0.052$. 357

APPENDIX C: EVOLUTION OF THE DRAG COEFFICIENT WITH THE REYNOLDS NUMBER 360

As stated in Sec. III A, at the smallest speed studied, for our scale models, we have $\text{Re} = 2.24 \times 10^5$, whereas for human swimmers, we have $\text{Re} = 3 \times 10^7$. Therefore, we have to make sure 361

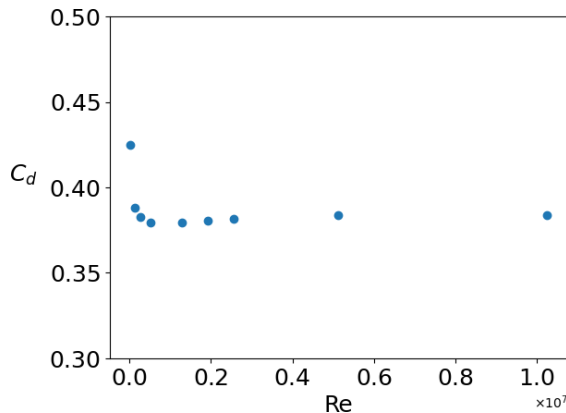


FIG. 19. Variation of the drag coefficient with the Reynolds number.

363 that the drag coefficient is independent from the Reynolds number if we want to generalize our
364 results to human swimmers. We performed CFD calculations on a fully submerged scale model
365 using OpenFoam as presented in Sec. III B. We changed the speed of the flow several times to change
366 the Reynolds number. We chose to make this study using CFD as it allows us to explore a wider
367 range of flow speeds compared to laboratory measurements. The results are shown in Fig. 19. We
368 observe that the drag coefficient remains roughly constant for $Re \in [1.2 \times 10^5; 1 \times 10^7]$. Therefore,
369 our results can be generalized to human swimmers. Moreover, for a smaller Reynolds number,
370 $Re = 3.6 \times 10^4$, there is an increase of the drag coefficient, which may be the sign of the drag crisis.
371 However, no measurements or CFD calculations were performed at such low Reynolds number.

-
- [1] D. Weihs, The hydrodynamics of dolphin drafting, *J. Biol.* **3**, 8 (2004).
 - [2] P. B. S. Lissaman and C. A. Shollenberger, Formation flight of birds, *Science* **168**, 1003 (1970).
 - [3] D. Weihs, Hydromechanics of fish schooling, *Nature (London)* **241**, 290 (1973).
 - [4] B. Blocken, T. Defraeye, E. Koninckx, J. Carmeliet, and P. Hespel, CFD simulations of the aerodynamic drag of two drafting cyclists, *Comput. Fluids* **71**, 435 (2013).
 - [5] B. Blocken, T. van Druenen, Y. Toparlar, F. Malizia, P. Mannion, T. Andrianne, T. Marchal, G. J. Maas, and J. Diepens, Aerodynamic drag in cycling pelotons: New insights by CFD simulation and wind tunnel testing, *J. Wind Eng. Ind. Aerodyn.* **179**, 319 (2018).
 - [6] E. Gan, M. Fong, and Y. L. Ng, CFD analysis of slipstreaming and side drafting techniques concerning aerodynamic drag in NASCAR racing, *CFD Lett.* **12**, 1 (2020).
 - [7] J. C. Chatard and B. Wilson, Drafting distance in swimming, *Med. Sci. Sports Exerc.* **35**, 1176 (2003).
 - [8] J. R. Coast and C. A. Piatt, heart rate and lactate responses to swimming in various drafting positions, *J. Swimming Res.* **15**, 27 (2001).
 - [9] M. Janssen, B. D. Wilson, and H. M. Toussaint, Effects of drafting on hydrodynamic and metabolic responses in front crawl swimming, *Med. Sci. Sports Exerc.* **41**, 837 (2009).
 - [10] G. A. Borg, Psychophysical bases of perceived exertion, *Med. Sci. Sports Exerc.* **14**, 377 (1982).
 - [11] A. J. Silva, A. Rouboa, A. Moreira, V. M. Reis, F. Alves, J. P. Vilas-Boas, and D. A. Marinho, Analysis of drafting effects in swimming using computational fluid dynamics, *J. Sports Sci. Med.* **7**, 60 (2008).
 - [12] D. A. Marinho, V. M. Reis, F. B. Alves, J. P. Vilas-Boas, L. Machado, A. J. Silva, and A. I. Rouboa, Hydrodynamic drag during gliding in swimming, *J. Appl. Biomech.* **25**, 253 (2009).
 - [13] Z. M. Yuan, M. Li, C. Y. Ji, L. Li, L. Jia, and A. Incecik, Steady hydrodynamic interaction between human swimmers, *J. Roy. Soc. Interface* **16**, 20180768 (2019).
 - [14] J. Westerweel, K. Aslan, P. Pennings, and B. Yilmaz, Advantage of a lead swimmer in drafting, [arXiv:1610.10082](https://arxiv.org/abs/1610.10082).
 - [15] MIT, Marine hydrodynamics, Water waves, <https://web.mit.edu/13.021/demos/lectures/lecture19.pdf>.
 - [16] See Supplemental Material at <http://link.aps.org/supplemental/10.1103/PhysRevFluids.xx.xxxxxx> for the scale model geometry used to 3D print them. It is also the geometry used for CFD simulations.
 - [17] Phyling, Drahi-X-Novation Center, <https://www.phyling.fr/>.
 - [18] OpenFoam, <https://openfoam.org/> (2022).
 - [19] OpenFoam, k-omega Shear Stress Transport (SST), User Guide v2112, <https://www.openfoam.com/documentation/guides/latest/doc/guide-turbulence-ras-k-omega-sst.html> (2016–2017).